

# Enzyme-triggered deep tumor penetration of a dual-drug nanomedicine enables an enhanced cancer combination therapy

Lei Gu<sup>a,1</sup>, Zhenyu Duan<sup>a,1</sup>, Xue Li<sup>b</sup>, Xin Li<sup>b</sup>, Yinggang Li<sup>a</sup>, Xiaoling Li<sup>a</sup>, Gang Xu<sup>a,b,d</sup>, Peng Gao<sup>a,b</sup>, Hu Zhang<sup>c</sup>, Zhongwei Gu<sup>a,d</sup>, Jie Chen<sup>b</sup>, Qiyong Gong<sup>a,d,e</sup>, Kui Luo<sup>a,d,\*</sup>

<sup>a</sup> Huaxi MR Research Center (HMRRCC), Department of Radiology, Frontiers Science Center for Disease-Related Molecular Network, State Key Laboratory of Biotherapy, West China Hospital, Sichuan University, Chengdu, 610041, China

<sup>b</sup> Liver Transplant Center, Organ Transplant Center, Breast Center, Laboratory of Stem Cell Biology, Laboratory of Clinical Proteomics and Metabolomics, Institutes for Systems Genetics, National Clinical Research Center for Geriatrics, West China Hospital, Sichuan University, Chengdu, Sichuan, China

<sup>c</sup> Amgen Bioprocessing Centre, Keck Graduate Institute, Claremont, CA, 91711, USA

<sup>d</sup> Functional and Molecular Imaging Key Laboratory of Sichuan Province, Key Laboratory of Transplant Engineering and Immunology, NHC, Research Unit of Psychoradiology, Chinese Academy of Medical Sciences, Chengdu, 610041, China

<sup>e</sup> Department of Radiology, West China Xiamen Hospital of Sichuan University, Xiamen, 361000, Fujian, China

## ARTICLE INFO

### Keywords:

Proliferation inhibition  
Apoptosis  
Amphiphilic and block polymer-dendron conjugate  
Enhanced penetration  
Membrane flow  
Combination therapy

## ABSTRACT

Cancer cells could be eradicated by promoting generation of excessive intracellular reactive oxygen species (ROS) via emerging nanomedicines. However, tumor heterogeneity and poor penetration of nanomedicines often lead to diverse levels of ROS production in the tumor site, and ROS at a low level promote tumor cell growth, thus diminishing the therapeutic effect of these nanomedicines. Herein, we construct an amphiphilic and block polymer-dendron conjugate-derived nanomedicine (Lap@pOEGMA-b-p(GFLG-Dendron-Ppa), GFLG-DP/Lap NPs) that incorporates a photosensitizer, Pyrropephorbide a (Ppa), for ROS therapy and Lapatinib (Lap) for molecular targeted therapy. Lap, an epidermal growth factor receptor (EGFR) inhibitor that plays a role in inhibiting cell growth and proliferation, is hypothesized to synergize with ROS therapy for effectively killing cancer cells. Our results suggest that the enzyme-sensitive polymeric conjugate, pOEGMA-b-p(GFLG-Dendron-Ppa) (GFLG-DP), releases in response to cathepsin B (CTSB) after entering the tumor tissue. Dendritic-Ppa has a strong adsorption capacity to tumor cell membranes, which promotes efficient penetration and long-term retention. Lap can also be efficiently delivered to internal tumor cells to play its role due to the increased vesicle activity. Laser irradiation of Ppa-containing tumor cells results in production of intracellular ROS that is sufficient for inducing cell apoptosis. Meanwhile, Lap efficiently inhibits proliferation of remaining viable cells even in deep tumor regions, thus generating a significant synergistic anti-tumor therapeutic effect. This novel strategy can be extended to the development of efficient membrane lipid-based therapies to effectively combat tumors.

## 1. Introduction

ROS serves a pivotal role in the life cycle of tumor cells [1]. When the ROS levels exceed the threshold for normal physiological activities, DNA, proteins or lipids within tumor cells could be damaged or their compositions modified, eventually leading to apoptosis [2–4]. Exogenous interventions to increase the intracellular ROS level is a promising

strategy for cancer therapy [4]. One of such interventions is to develop nanomedicines for photodynamic therapy (PDT) and great progress has been made in the recent decade [5–9]. However, the complicated tumor microenvironment (TME) is often a challenging obstacle for nanomedicines. Insufficient accumulation and poor penetration of the therapeutic components incorporated in these nanomedicines are often seen at the solid tumor site, hampering their clinical application [10–13].

Peer review under responsibility of KeAi Communications Co., Ltd.

\* Corresponding author. Huaxi MR Research Center (HMRRCC), Department of Radiology, Frontiers Science Center for Disease-Related Molecular Network, State Key Laboratory of Biotherapy, West China Hospital, Sichuan University, Chengdu, 610041, China.

E-mail address: [luokui@scu.edu.cn](mailto:luokui@scu.edu.cn) (K. Luo).

<sup>1</sup> These authors contributed equally: Lei Gu and Zhenyu Duan.

<https://doi.org/10.1016/j.bioactmat.2023.02.015>

Received 11 January 2023; Received in revised form 12 February 2023; Accepted 14 February 2023

2452-199X/© 2023 The Authors. Publishing services by Elsevier B.V. on behalf of KeAi Communications Co. Ltd. This is an open access article under the CC BY-NC-ND license (<http://creativecommons.org/licenses/by-nc-nd/4.0/>).

For example, heterogeneity of tumor tissues and nonuniformity in the distribution of therapeutic drugs result in different ROS production levels throughout the entire solid tumors. A variety of ROS-related signaling pathways could be activated, among which the downstream molecules in some of these signaling pathways may stimulate cells to build self-defense mechanisms to maintain cell survival or promote cell proliferation, thus diminishing the therapeutic effect of the nanomedicines [14–17]. Therefore, it is critical to improve insufficient localized bioavailability of drugs to overcome poor penetration of therapeutic agents for ROS-based antitumor therapy. In addition, the combination of molecular targeted therapy for tumor cell growth and proliferation with the ROS therapeutic modality may completely suppress tumor cell growth [18–20]. Lap, an inhibitor for EGFR, can inhibit EGFR autophosphorylation and block its signal transduction, and it is often employed as a therapeutic agent for inhibiting growth and proliferation of tumor cells [21–23]. Meanwhile, EGFR is overexpressed in many solid tumors, and its expression level is closely associated with the hypoxic level of the TME [24–26]. Since the hypoxic area is often located in the central region of tumor tissues, Lap-incorporated nanomedicines with weak tumor penetration ability cannot effectively deliver Lap to the hypoxic area to exert its therapeutic effect [27–31]. Therefore, an effective delivery system for Lap is pursued to achieve efficient penetration and high accumulation in the tumor tissues. Meanwhile, the delivery system could also deliver therapeutic agents to induce ROS-mediated apoptosis, resulting in a synergistic therapeutic effect against tumor cells.

Previously, we reported a nanomedicine for PDT derived from an amphiphilic and block polymer-dendron conjugate [32]. This CTSB-responsive nanomedicine could dissociate into dendritic-Ppa in tumor tissues. The dendritic-Ppa segment stably binds to the cell membranes, resulting in efficient deep penetration and long-term retention in tumors via the membrane flow. In this process, dendritic-Ppa embedded in the tumor membrane can damage the membrane structure and impair its inherent function, thus destroying this barrier that prevents internalization and penetration of anti-tumor drugs [32–35]. In addition, the linear-dendritic and block copolymers have been shown to improve stability and self-assembly of polymeric drug delivery systems. They have been successfully employed to co-deliver drugs to accomplish combination therapy [36,37]. In this

study, the CTSB-responsive nanomedicine for PDT was employed to load Lap, which could improve accumulation and penetration of Ppa and Lap in the tumor tissue and enhance their therapeutic effects including ROS-mediated tumor apoptosis and Lap-mediated proliferate inhibition, thus prolonging the survival duration of tumor-bearing mice, promoting efficient tumor clearance and preventing tumor metastasis. Our experimental results show that co-penetration of Lap and Ppa in the CTSB-responsive nanomedicine can significantly increase their combination therapeutic effect, and this co-delivery strategy into deep tumor tissues can be extended to the development of intelligent polymeric nanomedicines to combat cancer (Fig. 1).

## 2. Results and discussion

### 2.1. Formulation and characterizations of GFLG-DP/Lap NPs

The synthesis routes for the amphiphilic and block polymer-dendron-Ppa conjugate with enzyme-responsive GFLG linkers, GFLG-DP, and its control group, pOEGMA-b-p(Dendron-Ppa) (DP) without enzyme-responsive linkers, are shown in the Supporting Information (Figs. S1 and S2), and more information can be found in our previous article [32]. The molecular weight (MW) of GFLG-DP is 34.2 kDa with PDI of 1.18 and the Ppa loading rate is 4.92 wt%, and DP has a similar MW as well as an equivalent drug loading rate (34.2 kDa, PDI = 1.16, 5.03 wt% Ppa). The critical micelle concentration (CMC) value of GFLG-DP and DP is measured to be 10.30  $\mu\text{g/mL}$  and 16.44  $\mu\text{g/mL}$ , respectively, using pyrene as a fluorescence probe (Fig. S3), indicating both GFLG-DP and DP could self-assemble to form micelles and they have potential to encapsulate hydrophobic drugs.

Next, we utilized GFLG-DP and DP to encapsulate Lap via a thin film hydration method to construct dual-drug co-delivery nanoparticles (NPs), GFLG-DP/Lap NPs and Lap@pOEGMA-b-p(Lys-Dendron-Ppa) (DP/Lap NPs), respectively. The size distribution changes of GFLG-DP/Lap NPs and DP/Lap NPs at different feeding ratios of Lap are shown in Table S1, and the changes in the particle size before and after drug loading confirm successful loading of Lap to NPs. High performance liquid chromatography (HPLC) analysis was utilized to characterize the Lap content in both NPs (Fig. S4). There is a distinct peak for Lap in GFLG-DP/Lap NPs and DP/Lap NPs at a retention time of 6.00 min.

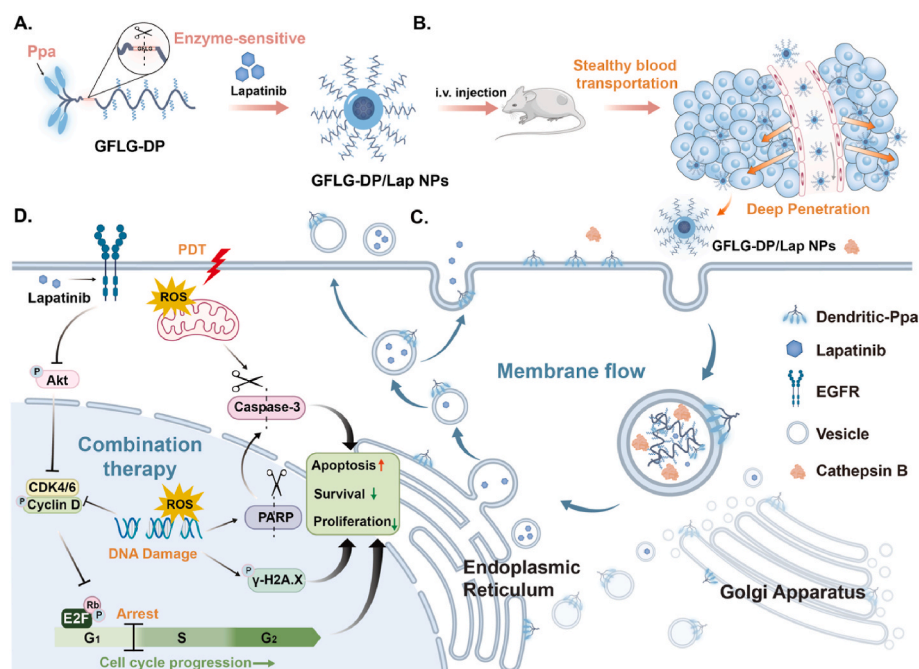


**Fig. 1.** Schematic illustration of the enzyme-sensitive block polymer-dendron conjugate-derived nanomedicine (GFLG-DP/Lap NPs) for a synergistic antitumor therapeutic effect by inducing apoptosis and inhibiting cell proliferation. (A): GFLG-DP could load Lapatinib, an EGFR inhibitor, to form a stable nanomedicine (GFLG-DP/Lap NPs). (B): GFLG-DP/Lap NPs display co-delivery of Ppa and Lap deep in the tumor tissue, which is realized by strong membrane activity. (C): Generated dendritic-Ppa from GFLG-DP could bind to cellular membranes and stimulate strong vesicle activity, facilitating intracellular and extra-cellular co-transportation of Ppa and Lap. (D): GFLG-DP/Lap NPs show a combined therapeutic effect by inducing apoptosis and inhibiting cell proliferation.

Meanwhile, the high resolution mass spectrometer (HRMS) result also confirms the presence of Lap in both NPs. The equivalent Lap loading is achieved for both DP NPs and GFLG-DP/Lap NPs by tuning the feed ratios, and the content ratio of Ppa and Lap in two NPs is kept at 5: 2 unless it is specifically stated.

Four NPs, including DP NPs, DP/Lap NPs, GFLG-DP NPs and GFLG-DP/Lap NPs, are monodispersed, and their hydrodynamic size is 217

nm, 186 nm, 145 nm, and 192 nm, respectively, via dynamic light scattering (DLS) (Fig. 2B, Fig. S5, Table S1). Transmission electron microscopy (TEM) images confirm that both GFLG-DP NPs and GFLG-DP/Lap NPs have a size of around 150 nm, which is similar to their DLS results (Fig. 2C). In addition, superposition peaks of Lap and the GFLG-DP or DP conjugate can be seen in the UV spectrum of GFLG-DP/Lap NPs or DP/Lap NPs, indicating successful loading of Lap into GFLG-DP and

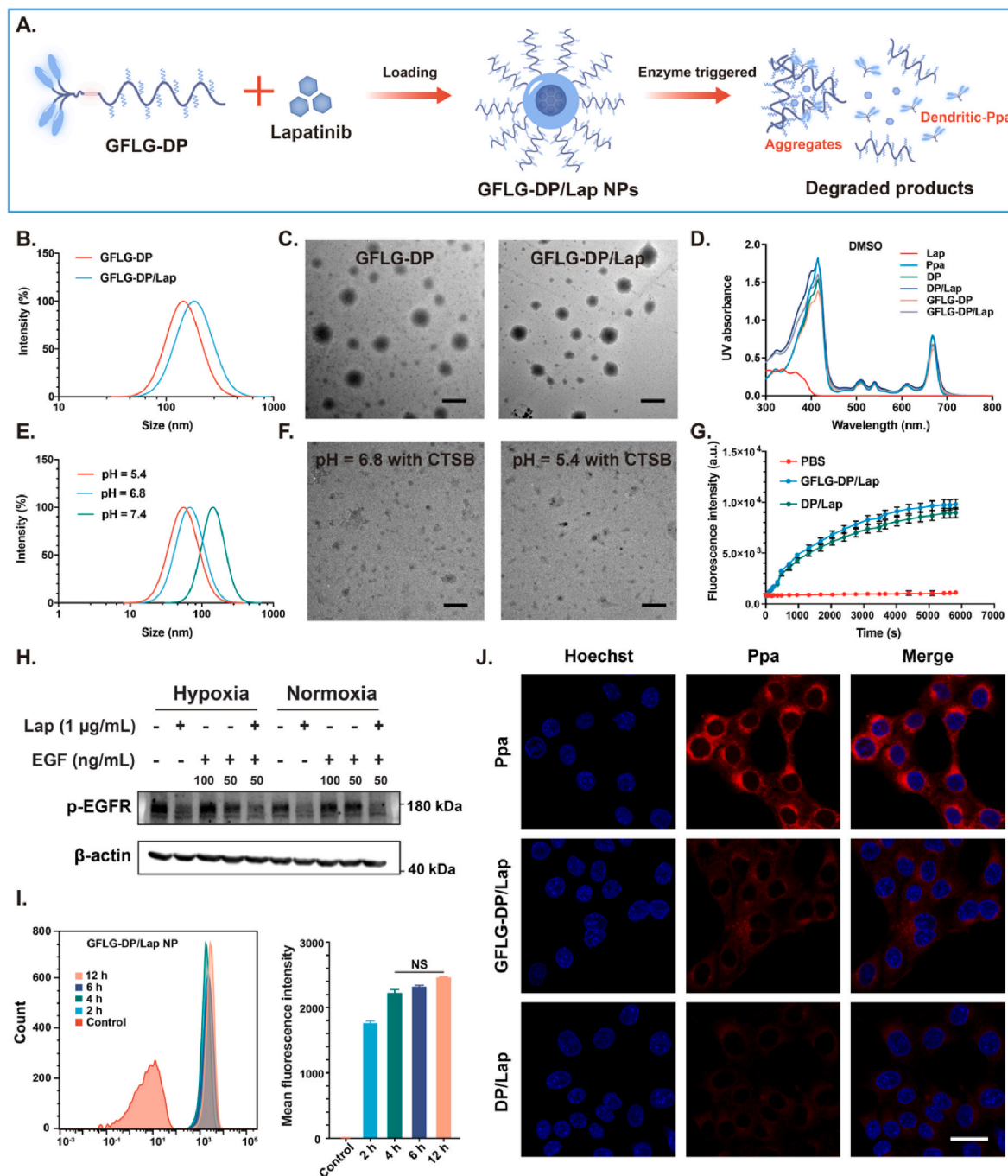


**Fig. 2.** (A): A schematic diagram of preparation and assembly of GFLG-DP/Lap NPs. (B): Hydrodynamic size of GFLG-DP NPs and GFLG-DP/lap NPs. (C): Typical TEM images of GFLG-DP NPs and GFLG-DP/lap NPs. Scale bar: 200 nm. (D): UV spectra of Ppa, Lap, DP, GFLP, DP/Lap and GFLP-DP/Lap NPs in DMSO. (E): Hydrodynamic size changes of GFLG-DP/Lap NPs in a simulated microenvironment at different pH values. (F): Typical TEM images of degraded GFLG-DP/Lap NPs at pH 6.8 or pH 5.4. (G): Fluorescence signal changes of SOSG in PBS containing DP/Lap NPs or GFLG-DP/Lap NPs upon exposure to a 660 nm laser for 100 min ( $n = 3$ ). (H): Western blots of p-EGFR in 4T1 cells under hypoxic/normoxia conditions after the treatment with Lap (1  $\mu$ g/mL) or EGF (50 ng/mL or 100 ng/mL) via immunoblot assays. (I): Flow cytometry of 4T1 cells treated with GFLG-DP/Lap NPs and their median fluorescence intensity (MFI) at 2, 4, 6 and 12 h ( $n = 3$ ). (J): Representative CLSM images for cellular uptake of free Ppa, DP NPs, DP/Lap NPs, GFLG-DP NPs and GFLG-DP/Lap NPs (equivalent Ppa: 5.0  $\mu$ g/mL) in 4T1 cells after 4 h of incubation. Scale bar: 20  $\mu$ m.

DP NPs (Fig. 2D).

GFLG-DP/Lap NPs, DP/Lap NPs, GFLG-DP NPs and DP NPs are very stable in the cell culture medium containing 10% fetal bovine serum for 6 days (Fig. S6), indicating their outstanding *in vitro* stability in a simulated physiological environment. However, after GFLG-DP/Lap NPs were incubated with CTSE in a McIlvaine's buffer for 24 h, they degrade into smaller segments with a hydrodynamic size of around 80 nm at pH = 5.4 or 100 nm at pH = 6.8 via DLS (Fig. 2E). Smaller spherical aggregates are also observed under TEM with a size of around 30 nm at pH = 5.4 or 50 nm at pH = 6.8 (Fig. 2F). After enzymatic cleavage of the GFLG linkers, the Ppa segments are released from the NPs. The encapsulated Lap escapes from the NPs, resulting in a smaller size. However, the dendritic-Ppa unit and Lap could be encapsulated by the loose nanostructure of the PEOGMA segment without Ppa after enzymatic fracture to form spherical aggregates<sup>32</sup>.

In addition, singlet oxygen green fluorescence probe (SOSG), which is highly sensitive to single-oxygen ( $^1\text{O}_2$ ), was utilized to assess the ROS generation of GFLG-DP/Lap NPs after laser irradiation and determine their efficacy as an agent for PDT. Compared with the  $^1\text{O}_2$  production from DP/Lap NPs in a neutral PBS solution, GFLG-DP/Lap NPs have generated more  $^1\text{O}_2$  with much stronger fluorescence intensity after 100 min of laser irradiation (660 nm, 10 mW/cm<sup>2</sup>) (Fig. 2G). Furthermore, we measured the fluorescence intensity of SOSG in the buffer containing CTSE in the presence of two NPs. After enzymatic degradation of the GFLG segment, a higher amount of  $^1\text{O}_2$  is produced from GFLG-DP/Lap NPs compared to DP/Lap NPs in a buffer (Fig. S7). These results indicate GFLG-DP/Lap NPs have a better  $^1\text{O}_2$  production performance than DP/Lap NPs, and they can achieve a greater PDT effect after enzymatic hydrolysis.

EGFR-positive murine mammary carcinoma (4T1) cells were employed to assess the curative effect of GFLG-DP/Lap NPs. The phosphorylation of EGFR (p-EGFR) in 4T1 cells was first assessed. In a hypoxia environment, there is a 2.3-fold increase in p-EGFR expression in 4T1 cells, while the addition of Lap decreases the p-EGFR level under both normoxia and hypoxia conditions (Fig. 2H and S8). Next, to examine the uptake of GFLG-DP/Lap NPs by 4T1 tumor cells, we co-incubated 4T1 cells with GFLG-DP/Lap NPs at the same concentration but for different durations. The fluorescence signal inside cells indicates that these NPs are efficiently internalized by 4T1 cells after 4 h (Fig. 2I). Additionally, 4T1 cells incubated with GFLG-DP NPs or GFLG-DP/Lap NPs for 4 h had considerably stronger Ppa fluorescence signals than cells treated with DP NPs or DP/Lap NPs (Fig. 2J and S9). These results suggest that GFLG-DP/Lap NPs have a high internalization rate into 4T1 cells, and the uptake pathways for GFLG-DP/Lap NPs and DP/Lap NPs by 4T1 cells are distinctly different. Since CTSE is extracellularly secreted in malignant tumor cells, dendritic Ppa may be released from GFLG-DP/Lap NPs after their exposure to CTSE in the extracellular microenvironment, thereby improving their cellular internalization.

## 2.2. ROS generation and cell death induction via GFLG-DP/Lap NPs

The generation of intracellular ROS induced by internalized GFLG-DP/Lap NPs was assessed via 2', 7'-dichlorofluorescein diacetate (DCFH-HA) in 4T1 cells [38]. As shown in Fig. 3A, after laser treatment, the presence of free Ppa strongly increases the ROS level in 4T1 cells. Compared with the control groups and non-irradiation groups, the ROS production in 4T1 cells after incubation with DP/Lap NPs or GFLG-DP/Lap NPs under laser irradiation is significantly raised, which is also evidenced from flow cytometry analysis (Fig. 3B).

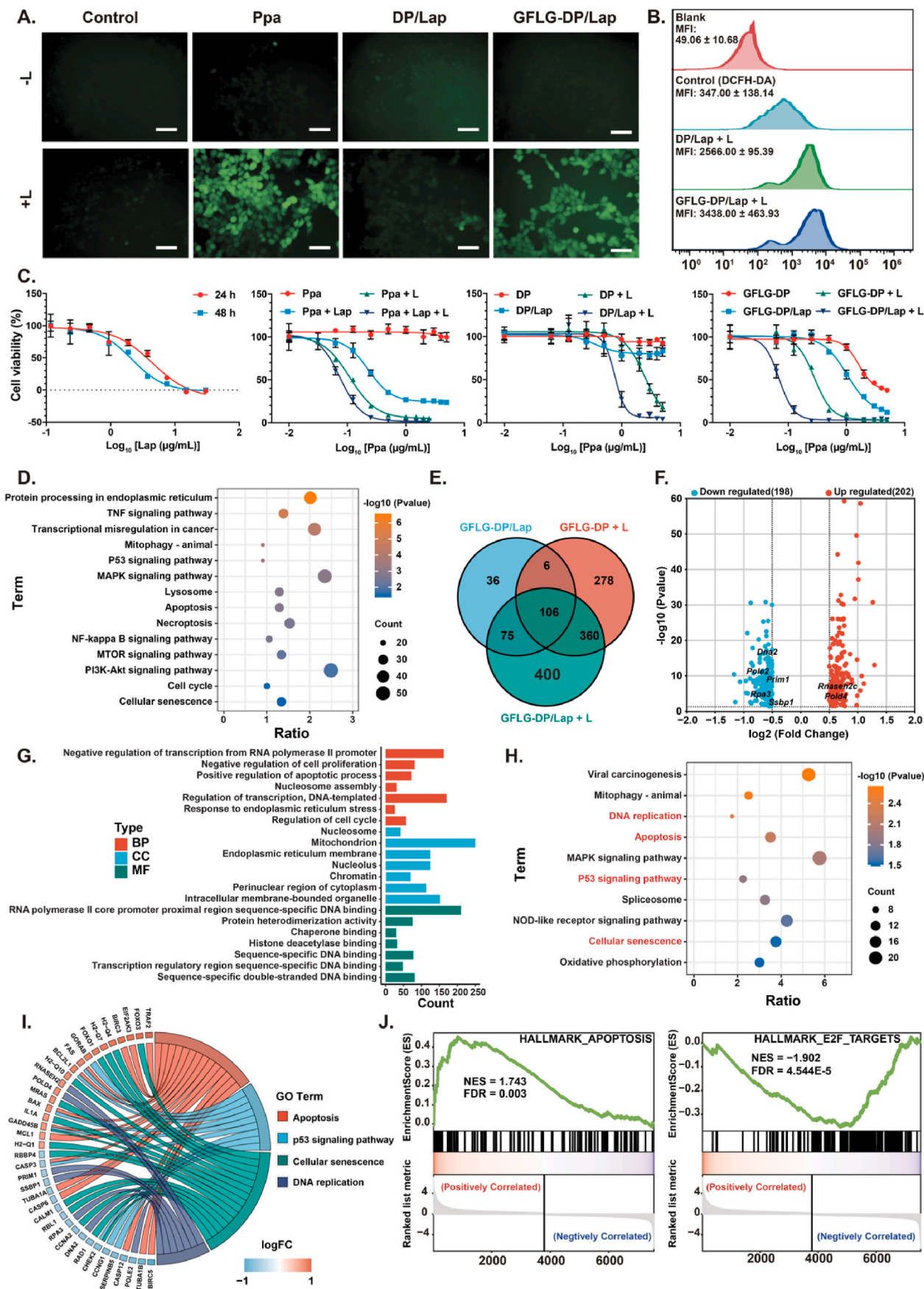
Next, the cellular viability of 4T1 cells treated with GFLG-DP/Lap NPs or DP/Lap NPs, with or without irradiation treatment, was examined via the CCK-8 assay (Fig. 3C). The viability of cells treated with free Lap gradually decreases, and the IC<sub>50</sub> value of free Lap is 4.41 μg/mL and 2.02 μg/mL at 24 h and 48 h, respectively. Treatment with DP NPs or DP/Lap NPs within the test concentration range does not impact the viability of tumor cells. In contrast, the cell viability is less than 40%

after treatment with GFLG-DP NPs at the highest concentration (5.0 μg equivalent Ppa/mL), and below 20% after treatment with GFLG-DP/Lap NPs at the same concentration. After laser irradiation (660 nm, 1.0 J/cm<sup>2</sup>), cells incubated with free Ppa, DP NPs, GFLG-DP NPs, DP/Lap NPs or GFLG-DP/Lap NPs exhibit Ppa concentration-dependent cytotoxicity. It is worth noting that GFLG-DP NPs (IC<sub>50</sub>: 0.27 μg/mL) have a more cytotoxic effect than DP NPs (IC<sub>50</sub>: 2.47 μg/mL) on 4T1 cells at an equivalent Ppa concentration under the same laser irradiation condition, which may be attributed to a high level of internalization and ROS generation of GFLG-DP NPs. Compared to PDT via DP NPs and GFLG-DP NPs, the incorporation of Lap into both NPs enhances the toxicity to tumor cells after laser irradiation. The IC<sub>50</sub> values of DP/Lap NPs and GFLG-DP/Lap NPs with laser treatment against 4T1 cells are 0.76 μg/mL and 0.12 μg/mL, respectively. These results support that the combination of PDT and Lap treatment could exert an excellent synergistic antitumor effect *in vitro*.

## 2.3. GFLG-DP/Lap NPs induce apoptosis and block cell proliferation

To probe the molecular mechanism of GFLG-DP/Lap NPs under laser irradiation, we used transcriptome sequencing to analyze the differences in mRNA expression in tumor cells after treatment with GFLG-DP/Lap NPs, compared with other control groups. Compared to control cells without exposure to GFLG-DP/Lap NPs, the heatmap and volcano map reveal differential expressed genes (DEGs) in tumor cells treated with GFLG-DP/Lap NPs with laser irradiation (Fig. S10 A and S10 B). DEGs enrichment results suggest that genes associated with the cell death and proliferation pathways are significantly changed in cells after treatment of GFLG-DP/Lap NPs with laser irradiation, including the TNF signaling pathway, the MAPK signaling pathway, the p53 signaling pathway, apoptosis, necroptosis, the NF-kappa B pathway, the MTOR signaling pathway, the PI3K-Akt signaling pathway, cell cycle and cellular senescence (Fig. 3D). Compared with the treatment groups by GFLG-DP NPs with laser and GFLG-DP/Lap NPs without laser, 400 DEGs are specifically identified in cells after treatment of GFLG-DP/Lap NPs with irradiation (Fig. 3E). Among them, 202 genes are upregulated and 198 genes downregulated (Fig. 3F). Gene Ontology (GO) term enrichment analysis demonstrates that regulated genes after treatment of GFLG-DP/Lap NPs with laser irradiation are predominantly involved in negative regulation of cell proliferation and positive regulation of apoptosis (Fig. 3G). Consistent with the enrichment results in Fig. 3D, functional enrichment analysis supports that these screened regulated genes are associated with the signaling pathways related to cell survival and proliferation processes (Fig. 3H). It is worth noting that the combination treatment has a significant impact on key genes (*rnaseh2c*, *pold4*, *ssbp1*, *dna2*, *rpa3*, *pole2* and *prim1*) for DNA replication and genome stability (Fig. 3F and I). To gain further insights at the gene-set level, we performed gene set enrichment analysis (GSEA) of the differential genes in the cells between the group treated with GFLG-DP/Lap NPs with laser irradiation and the control group without exposure to GFLG-DP/Lap NPs. Consistently, the gene sets associated with apoptosis (NES = 1.74, FDR = 0.00), the P53 pathway (NES = 2.09, FDR = 0.00), and the TNFA signaling pathway (NES = 2.96, FDR = 0.00) have a significantly positive enrichment score in the cells after treatment with GFLG-DP/Lap NPs and laser irradiation. Meanwhile, a negative enrichment score is identified in these signatures including the E2F targets pathway (NES = -1.90, FDR = 0.00) and the G2M checkpoint (NES = -1.48, FDR = 0.00) (Fig. 3J and Fig. S11). Therefore, these data suggest that GFLG-DP/Lap NPs under laser irradiation have an efficacious combinational therapeutic effect on cell killing and growth inhibition.

We further investigated the role of apoptosis and the DNA replication pathway in the combination therapy of PDT plus Lap treatment. We first examined the acute damage to tumor cells due to ROS production. As shown in Fig. 4A and Fig. S12, the treated tumor cells in the GFLG-DP NPs and GFLG-DP/Lap NPs groups are rapidly killed within a short period of time after laser irradiation. This is accompanied with a rapid



(caption on next page)

**Fig. 3.** (A): Intracellular ROS generation in 4T1 cells after incubation with free Ppa, DP/Lap NPs and GFLG-DP/Lap NPs at 1.0  $\mu\text{g}$  equivalent Ppa/mL with or without 660 nm laser irradiation (1.0  $\text{J}/\text{cm}^2$ ) via the DCFH probe. Scale bar: 50  $\mu\text{m}$ . (B): MFI of DCFH in the 4T1 cells after different treatments in (A) ( $n = 3$ ). (C): Cytotoxicity of Lap against 4T1 cells at 24 h and 48 h (first); Cytotoxicity of different formulations against 4T1 tumor cells ( $n = 3$ ), including Ppa, Ppa with laser irradiation, Ppa + Lap, Ppa + Lap with laser irradiation (second); DP NPs, DP NPs with laser irradiation, DP/Lap NPs, DP/Lap NPs with laser irradiation (third); GFLG-DP NPs, GFLG-DP NPs with laser irradiation, GFLG-DP/Lap NPs, and GFLG-DP/Lap NPs with laser irradiation (fourth). (D): Top 14 enriched KEGG pathways in cells treated with GFLG-DP/Lap NPs and laser irradiation compared to the blank control via functional enrichment analysis. (E): Venn diagram of the DEGs in cells treated with GFLG-DP/Lap NPs, GFLG-DP NPs with irradiation and GFLG-DP/Lap NPs with irradiation. (F): Volcano plot of unique DEGs in the GFLG-DP/Lap laser irradiation cells (total number of DEGs = 400, the number of downregulated genes = 198, the number of upregulated genes = 202). (G): Enriched GO terms from 400 DEGs via functional enrichment analysis. Red for biological process (BP), blue for cellular component (CC) and green for molecular function (MF). (H): Functional enrichment analysis of these 400 DEGs in (F). KEGG analysis shows that the cell proliferation and survival processes are significantly affected. (I): Chord diagram for specific biological processes related to selective DEGs in (F). (J): Positive enrichment scores for the apoptosis pathway and negative enrichment scores for the E2F targets pathway from GSEA of cells treated with GFLG-DP/Lap NPs and irradiation.

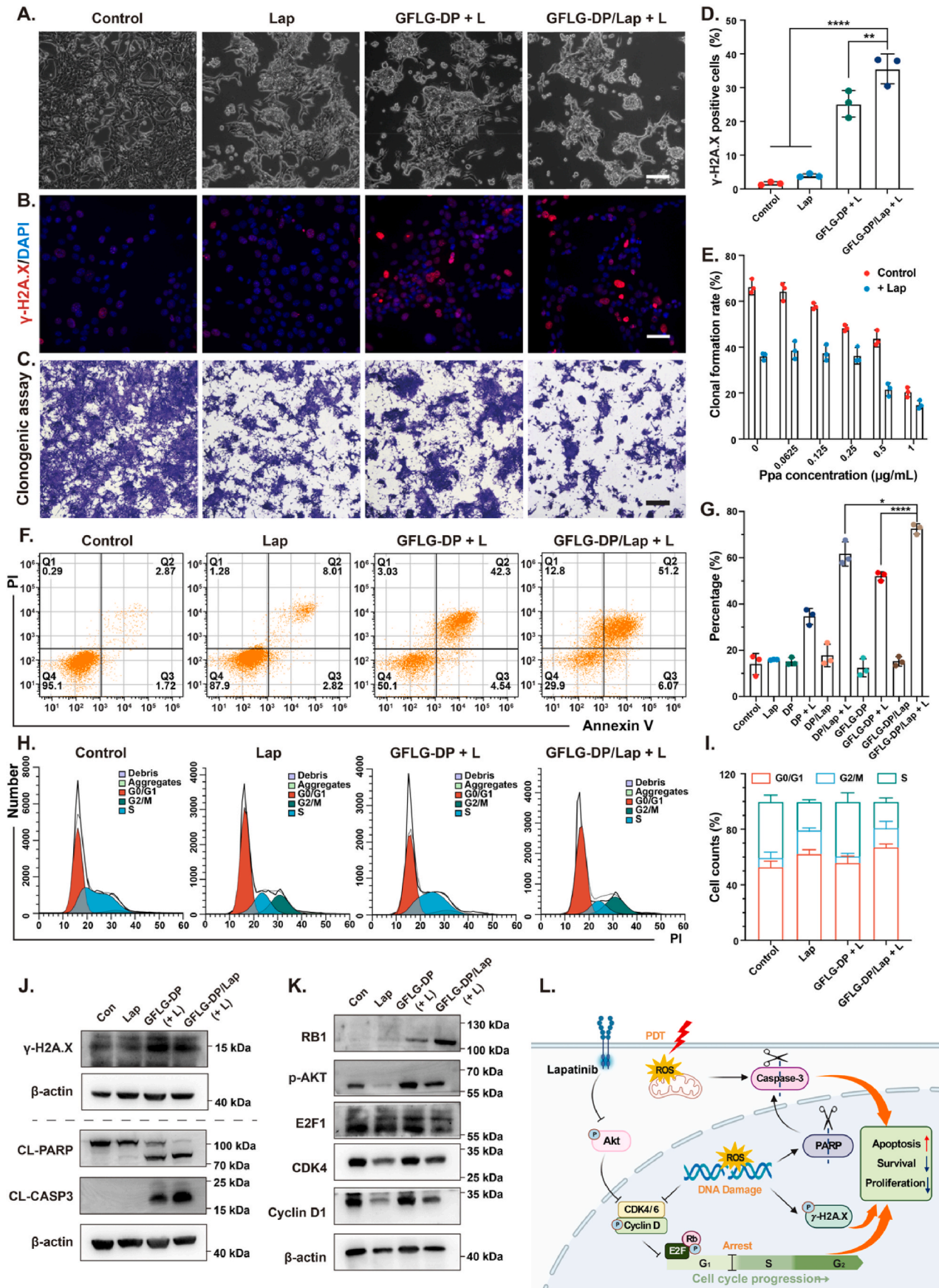
increase in the level of  $\gamma\text{-H2AX}$  foci in the nucleus of the irradiated cells, indicating that a great amount of ROS induced by PDT can instantly cause DNA damage (Fig. 4B and D). These results are also supported from immunoblot assays (Fig. 4J). Meanwhile, the addition of Lap into GFLG-DP NPs contributes to an increase in the cell mortality, which is consisted with the apoptosis analyses by flow cytometry and immunoblot assays. Compared with non-irradiation groups, treatment with DP NPs or GFLG-DP NPs and laser irradiation leads to an increase in the 4T1 cellular apoptosis ratio determined by flow cytometry, and the apoptotic cells subject to DP NPs with irradiation account for  $34.60 \pm 3.44\%$  of total cells, while  $52.06\% \pm 1.92\%$  in the group subject to GFLG-DP NPs with irradiation (Figs. S13 and S14). Most impressively, the percentage of apoptotic cells increases to  $72.52\% \pm 2.21\%$  in the group treated with GFLG-DP/Lap NPs and irradiation compared with  $52.06\% \pm 1.92\%$  in the group treated with GFLG-DP NPs and laser radiation, confirming the combinational pro-apoptotic effect of PDT and Lap therapy (Fig. 4F and G). Immunoblot analysis supports that the key apoptosis-related proteins in tumor cells including cleaved caspase-3 (CL-CASP3) and cleaved PARP (CL-PARP) are upregulated after treatment with irradiation and GFLG-DP NPs or GFLG-DP/Lap NPs. GFLG-DP/Lap NPs-treated cells show a higher expression level of these apoptosis-related proteins compared with those treated with GFLG-DP NPs under the same laser irradiation condition (Fig. 4J and S16).

Given the enhanced activation of EGFR in 4T1 cells under a hypoxic condition (Fig. 2H), we speculated that tumor cells could maintain rapid growth without sufficient irradiation. As shown in Fig. S15, colony formation assays confirm that colony formation from 4T1 cells after treatment with a low dose of Ppa (0.0625  $\mu\text{g}/\text{mL}$ ) under laser irradiation (0.5  $\text{J}/\text{cm}^2$ ) is similar to that of control cells. However, treatment with GFLG-DP/Lap NPs at the equivalent Ppa dose under the same laser irradiation condition significantly inhibits clonal formation of 4T1 tumor cells (Fig. 4C and S15). In addition, the results of cell cycle analysis show that the addition of Lap into GFLG-DP NPs significantly reduces the number of S-phase cells, while the number of G1-phase and G2/M-phase cells increases (Fig. 4H and I). The G1 checkpoint arrest results are consistent with western blot analyses (Fig. 4K). The expression level of CDK4 and cyclin D1 proteins is reduced in the groups treated with free Lap and GFLG-DP/Lap NPs (with laser irradiation), and both proteins are associated with cell cycle in tumor cells. The reduction in the expression of both proteins results in a downstream effect: reducing activation of the RB-1 protein and blocking release of the E2F1 protein. Cell cycle assay results suggest that the combination of PDT and Lap treatment leads to cell cycle arrest in the G1 phase and blockage of cell division (Fig. 2L). Collectively, the results suggest that the *in vitro* PDT and Lap lethality on 4T1 cells is primarily due to a strong ROS-mediated cell killing effect and inhibition of EGFR-mediated activation of cell proliferation. The combined treatment can rapidly induce cell apoptosis and effectively inhibit the growth of the remaining viable tumor cells.

#### 2.4. GFLG-DP/Lap NPs serve as an effective nanomedicine for tumor inhibition

The therapeutic effect of GFLG-DP/Lap NPs for 4T1 tumors was evaluated in a subcutaneous mice model. Mice bearing subcutaneous 4T1 tumors received four doses of i.v. injections of saline, free Lap, free Ppa, DP NPs, DP/Lap NPs, GFLG-DP NPs or GFLG-DP/Lap NPs (the Ppa dose of 5.0 mg/kg, the Lap dose of 2.0 mg/kg,  $n = 10$  per group, except  $n = 5$  for saline and free Lap) and the scheduled injections are shown in Fig. 5A. Among them, one half of the mice with free Ppa, DP NPs, DP/Lap NPs, GFLG-DP NPs and GFLG-DP/Lap NPs were randomly selected for laser irradiation treatment at 24 h after injection of them. During treatment, the body weight and the tumor size of mice were measured every two days (Figs. S17 and S19). On day 17 after the first treatment, the tumors grow rapidly and the tumor diameter reaches 15 mm in the saline-treated mice, the experiment is terminated according to the international animal ethics guidelines. As shown in Fig. 5B, C, S17 and S18A, the mice in the saline-treated group have a 15.4-fold increase in the tumor volume at the end of treatment. Tumor growth is effectively suppressed in the nanomedicines/irradiation-treated mice groups, while treatment with free Ppa and irradiation results in a slightly efficacious effect on tumor-bearing mice with a 14.4-fold increase in the tumor volume, which may be due to a longer circulation time of nanomedicines, leading to the enrichment of photosensitizers in the tumor via the enhanced permeability and retention (EPR) effect of solid tumors. Treatment of mice with DP NPs, DP/Lap NPs and GFLG-DP NPs with laser irradiation exhibits a similar inhibition efficacy, resulting in a 3.9-fold, 3.6-fold and 3.5-fold increase in the tumor size, respectively. On the contrary, tumor progression is significantly inhibited in the mice treated with GFLG-DP/Lap NPs and laser irradiation with a 1.4-fold reduction in the original tumor volume, and their mean tumor volume is down to 60  $\text{mm}^3$  (Fig. S20). In addition, the average tumor weights from the mice after treatment support the pronounced therapeutic effect of GFLG-DP/Lap NPs with irradiation, and the tumor inhibition rate in these mice reaches 90% (Fig. 5D). Meanwhile, the therapeutic effect of GFLG-DP/Lap NPs with irradiation was evaluated with a long-term survival study in the 4T1 tumor model. The median survival of the saline group is 17 days, while the mice treated with GFLG-DP NPs (with laser irradiation) and DP/Lap NPs (with laser irradiation) show a moderate therapeutic efficacy with a median survival of 28 days and 31 days, respectively. The intervention with GFLG-DP/Lap NPs with laser irradiation effectively inhibits tumor growth, and the median survival of the group is extended to 39 days (Fig. 5E and S18B), 2.3 times longer than the saline group.

The antitumor effect of the combinational therapy was further supported by immunofluorescence analysis of tumor tissues. Terminal deoxynucleotidyl transferase-mediated deoxyuridine triphosphate nick end labeling (TUNEL) assays of the harvested tumors confirm that GFLG-DP NPs and GFLG-DP/Lap NPs with irradiation efficiently induce more late apoptotic cells compared with DP NPs or DP/Lap NPs (Fig. 5F and G). However, the introduction of Lap into GFLG-DP NPs does not significantly increase the percentage of late apoptotic tumor cells *in vivo*. Furthermore, Ki67 expression in the mice receiving GFLG-DP/Lap NPs is



(caption on next page)

**Fig. 4.** (A): Typical cell morphologies of 4T1 cells treated with Lap (0.4  $\mu\text{g}/\text{mL}$ ), GFLG-DP NPs (1.0  $\mu\text{g}$  equivalent Ppa/mL) and GFLG-DP/Lap NPs (1.0  $\mu\text{g}$  equivalent Ppa/mL) under laser irradiation (1.0  $\text{J}/\text{cm}^2$ ). Scale bar: 50  $\mu\text{m}$ . (B): The  $\gamma\text{-H2AX}$  foci content in the nucleus of 4T1 cells after treatments in (A). Scale bar: 50  $\mu\text{m}$ . (C): Representative colony formation assay results of 4T1 cells after treatment with Lap (0.2  $\mu\text{g}/\text{mL}$ ), GFLG-DP NPs (0.5  $\mu\text{g}$  equivalent Ppa/mL) and GFLG-DP/Lap NPs (0.5  $\mu\text{g}$  equivalent Ppa/mL) under laser irradiation (0.5  $\text{J}/\text{cm}^2$ ) for 48 h. Scale bar: 50  $\mu\text{m}$ . (D): Percentage of  $\gamma\text{-H2AX}$ -positive cells after different treatments in (B) ( $n = 3$ ). \*\* $P < 0.01$  and \*\*\*\* $P < 0.0001$ . (E): Clonal formation rate after different treatments in (C) ( $n = 3$ ). (F): Apoptosis analysis of 4T1 cells treated with different methods by flow cytometry ( $n = 3$ ) including the blank control, Lap (0.2  $\mu\text{g}/\text{mL}$ ), GFLG-DP NPs (0.5  $\mu\text{g}$  equivalent Ppa/mL) and GFLG-DP/Lap NPs (0.5  $\mu\text{g}$  equivalent Ppa/mL) with laser irradiation (1.0  $\text{J}/\text{cm}^2$ ). (G): The apoptotic percentage of 4T1 cells with various treatments ( $n = 3$ ). \* $P < 0.05$  and \*\*\*\* $P < 0.0001$ . (H): Cell cycle analysis of 4T1 cells after different treatments in (C). Cell cycle alteration may be in response to the DNA damage induced by the combination treatment. (I): The percentage of cells in each phase of cell cycle ( $n = 3$ ). (J): Immunoblots of  $\gamma\text{-H2AX}$ , cleaved PARP and cleaved caspase 3 in 4T1 cells after treatments in (A). (K): Immunoblots of proteins for cell cycle progression, including p-AKT, CDK4/6, cyclin D1, E2F and RB1, in 4T1 cells after treatments in (C). (L): Schematic diagram for the mechanisms of the combination effect of Lap therapy and PDT against 4T1 cells.

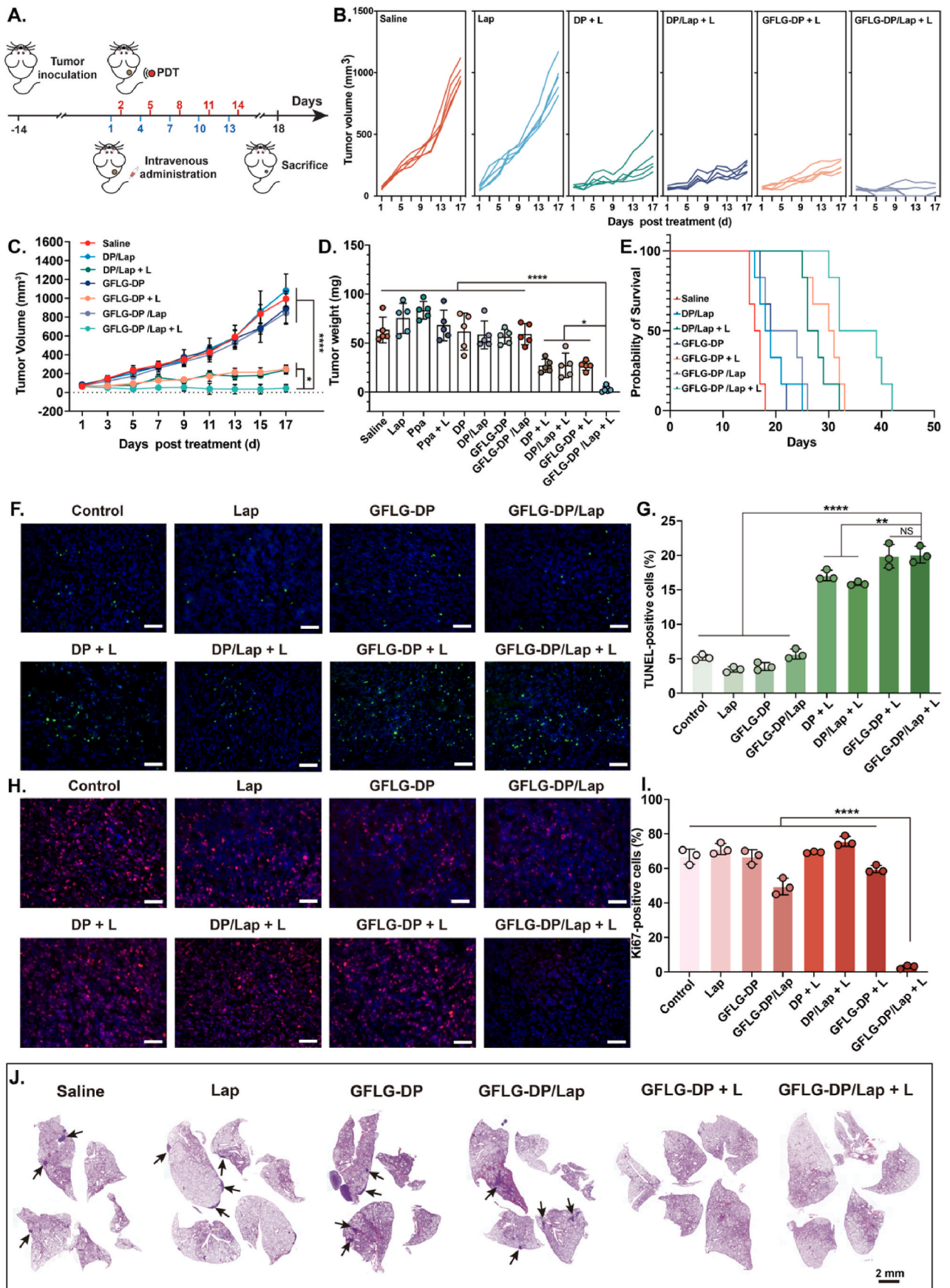
significantly reduced after irradiation compared with that in other groups, indicating the proliferation of remaining tumor cells is significantly inhibited after the combination therapeutic treatment by GFLG-DP/Lap NPs with irradiation (Fig. 5H and I). There is no statistical difference of the Ki67 expressions between the groups treated with DP NPs with irradiation and DP/Lap NPs with irradiation, suggesting an unsatisfactory anti-tumor effect of DP/Lap NPs with irradiation. H&E staining images of lungs confirm a great anti-tumor metastasis effect after treatment with GFLG-DP/Lap NPs and laser irradiation, which is ascribed to the induction of tumor cell apoptosis and proliferation inhibition (Fig. 5J and S21). These results indicate that co-delivery of drugs via nanomedicines into the tumor site does not guarantee an effective combination effect of PDT and Lap, such as DP/Lap NPs. Based on our previous report<sup>32</sup>, dendritic-Ppa released from GFLG-DP NPs in the tumor site could bind to the cell membrane systems, achieving deep tumor penetration of Ppa through the membrane flow. This process may also promote the penetration of the co-delivered Lap in GFLG-DP/Lap NPs. Deep penetration of both drugs in solid tumors could contribute to such a promising efficacy in tumor growth inhibition and metastasis suppression.

### 2.5. GFLG-DP/Lap NPs achieve co-delivery into deep tumors via membrane activity

The above experimental data support that GFLG-DP/Lap NPs not only have a better PDT effect, but also a significantly inhibitory effect on tumor proliferation compared with other formulations. It is well accepted that the distribution of EGFR is impacted by the degree of hypoxia in the tumor environment, which is closely correlated with the depth of solid tumors. We hypothesized that the outstanding therapeutic result of GFLG-DP/Lap NPs may be ascribed to spacious distribution of the loaded Lap throughout the tumor tissues, especially in the central tumor regions, and the interaction between the nanomedicine and the tumor cell membrane could be a contributing factor to this process according to our previous study<sup>32</sup>. The CTSB-sensitive polymeric carrier has been demonstrated to release the dendritic-Ppa unit at the tumor site, and the released dendritic-Ppa unit can disrupt the tumor cell membrane and thus deeply penetrate into the tumor tissue via cellular interaction. The interaction between GFLG-DP/Lap NPs and the tumor cell membrane may facilitate effective penetration of the encapsulated Lap. Herein, we first unitized isolated giant plasma membrane vesicles (GPMVs) from the 4T1 cells incubated with DP/Lap NPs or GFLG-DP/Lap NPs. Confocal laser scanning microscopy (CLSM) images show that the fluorescent signal of Ppa is evident on the GPMVs from the GFLG-DP/Lap NPs-treated group. Conversely, the fluorescent signal is barely detectable on the vesicles from the DP/Lap NPs-treated group, indicating that the degraded product from GFLG-DP/Lap NPs could be effectively bound to the cell membrane (Fig. 6A and B). Furthermore, the amount of dendritic-Ppa released from GFLG-DP/Lap NPs on the GPMVs from tumor cells pre-treated with a CTSB inhibitor is significantly reduced (Fig. S22). Meanwhile, in GFLG-DP/Lap NPs-treated murine brain microvascular endothelial cells (bEnd.3), dendritic-Ppa is barely bound or embedded in the cell membrane of bEnd.3 cells (Fig. S23). These results suggest that the dissociation of GFLG-DP/Lap

NPs depends on their response to CTSB in the tumor microenvironment and the dissociation is essential for the interaction between dendritic-Ppa and tumor cell membranes. It is noticed that the fluorescence intensity is retained on the GPMVs from 4T1 cells after removing the medium containing GFLG-DP/Lap NPs for 2 h, indicating that dendritic-Ppa could bind stably to the cell membrane (Fig. S24). Meanwhile, compared with the DP/Lap NPs group without degradation, GFLG-DP/Lap NPs have a higher degree of co-localization with the endoplasmic reticulum (ER) and Golgi apparatus (GA), indicating that their degraded products containing Ppa could be delivered intra- and extracellularly via the vesicular activity (Fig. 6C and D). Next, we unitized rhodamine-labeled dextran (70 kDa) or CF488A-labeled transferrin to identify the endocytosis pathways of NPs (Figs. S25 and S26). As shown in Fig. 6E and S25, the red fluorescence (Ppa) was overlapped with the green signal from rhodamine-dextran in the GFLG-DP/Lap-treated cells, indicating that dendritic-Ppa could induce strong cell membrane activities to form the ruffling on the membrane surface and enhance cellular internalization of NPs by the macropinocytosis pathway. Therefore, GFLG-DP/Lap NPs can utilize the membrane activity to deliver Ppa to neighboring cells, achieving deep tumor penetration. Fig. 6F describes the transportation process of GFLG-DP/Lap NPs, escape of their released photosensitizers and inhibitors out of treated cells and diffusion into solid tumors via their interaction with tumor cell membranes.

We also explored the cellular membrane interaction with GFLG-DP/Lap NPs to facilitate tumor penetration of the incorporated Lap. First, we examined the penetration ability of the NPs in the solid tumor tissue via *in vitro* three-dimensional (3D) multicellular tumor spheroids (MTSs) [39,40]. After 12 h incubation, the Ppa fluorescence signal of two NPs are seen inside the MTSs, and GFLG-DP/Lap NPs are more spatially distributed in 4T1 MTSs compared with DP/Lap NPs (Fig. 7A). Quantitative analysis of the fluorescence signal confirms that the overall fluorescence intensity of GFLG-DP/Lap NPs in the entire MTSs layer (60  $\mu\text{m}$ ) is much stronger than that in the DP/Lap NPs-treated group (Fig. 7B and C). These results support that GFLG-DP/Lap NPs could achieve effective penetration and accumulation in the MTSs. Next, we analyzed the distribution of Lap in 3D MTSs via desorption electrospray ionization mass spectrometry imaging (DESI-MSI) (Fig. 7D–G and S27) [41–43]. Fig. 7D and E are the results of DESI-MSI analysis of Lap in the MTSs after treatment with GFLG-DP/Lap NPs and DP/Lap NPs at the same Lap concentration, respectively. After 12 h of incubation with the MTSs, Lap in both DP/Lap NPs and GFLG-DP/Lap NPs-treated groups are detected, and the amount of Lap in the DP/Lap-treated MTSs is extremely low (Fig. 7 D-iii). However, Lap in the GFLG-DP/Lap NPs-treated group could diffuse and accumulate in the entire tumor spheroid (Fig. 7 E-iii), and the intensity of Lap in the GFLG-DP/Lap NPs-treated MTSs is significantly higher than that in the DP/Lap NPs-treated group. The MSI results demonstrate that the GFLG-DP carrier could promote the penetration of Lap in GFLG-DP/Lap NPs. Meanwhile, we analyzed the H&E staining images (Fig. 7E–i) and fluorescence images from the same samples. Consistent with previous results (Fig. 7A), strong Ppa fluorescence signal is observed in the tumor spheroids incubated with GFLG-DP/Lap NPs (Fig. 7E–ii), indicating that GFLG-DP/Lap NPs or their degraded products could be internalized by tumor cells and the



(caption on next page)

**Fig. 5.** (A): Schematic illustration of combinational therapy via GFLG-DP/Lap NPs to inhibit 4T1 tumors. On day 14 after tumor inoculation, mice were randomly divided into 12 groups (n = 5) and treated with intravenous administrations of saline, Lap, DP NPs, DP/Lap NPs, GFLG-DP NPs, GFLG-DP/Lap NPs (5.0 mg equivalent Ppa/kg mice; 2.0 mg equivalent Lap/kg mice) on the days indicated by blue. In the mice groups under laser irradiation, mice were irradiated on the days indicated by red (660 nm laser, 300 mW/cm<sup>2</sup> for 8 min). (B): Tumor growth curves of each individual mouse in different treatment groups in (A) (n = 5). (C): Tumor growth curves of tumor-bearing mice after various treatments in (A) (n = 5). \**P* < 0.05 and \*\*\*\**P* < 0.0001. (D): Tumor weights at the end of various treatments in (A) (n = 5). \**P* < 0.05 and \*\*\*\**P* < 0.0001. (E): Kaplan-Meier survival curves of mice in different treatment groups in (A). (F): TUNEL staining analysis of collected tumors. Green for apoptotic cells. Scale bar: 50 μm. (G): Percentage of TUNEL-positive cells in the tumors after different treatments in (A) (n = 3). \*\**P* < 0.01, \*\*\*\**P* < 0.0001 and ns = not significant. (H): Ki67 staining of tumors after different treatments in (A). Red for proliferating cells. Scale bar: 50 μm. (I): Percentage of Ki67-positive cells in the tumors after different treatments in (A) (n = 3). \*\*\*\**P* < 0.0001. (J): Representative H&E staining of the lung from mice after different treatments in (A). Arrows point to metastases. Scale bar: 2000 μm.

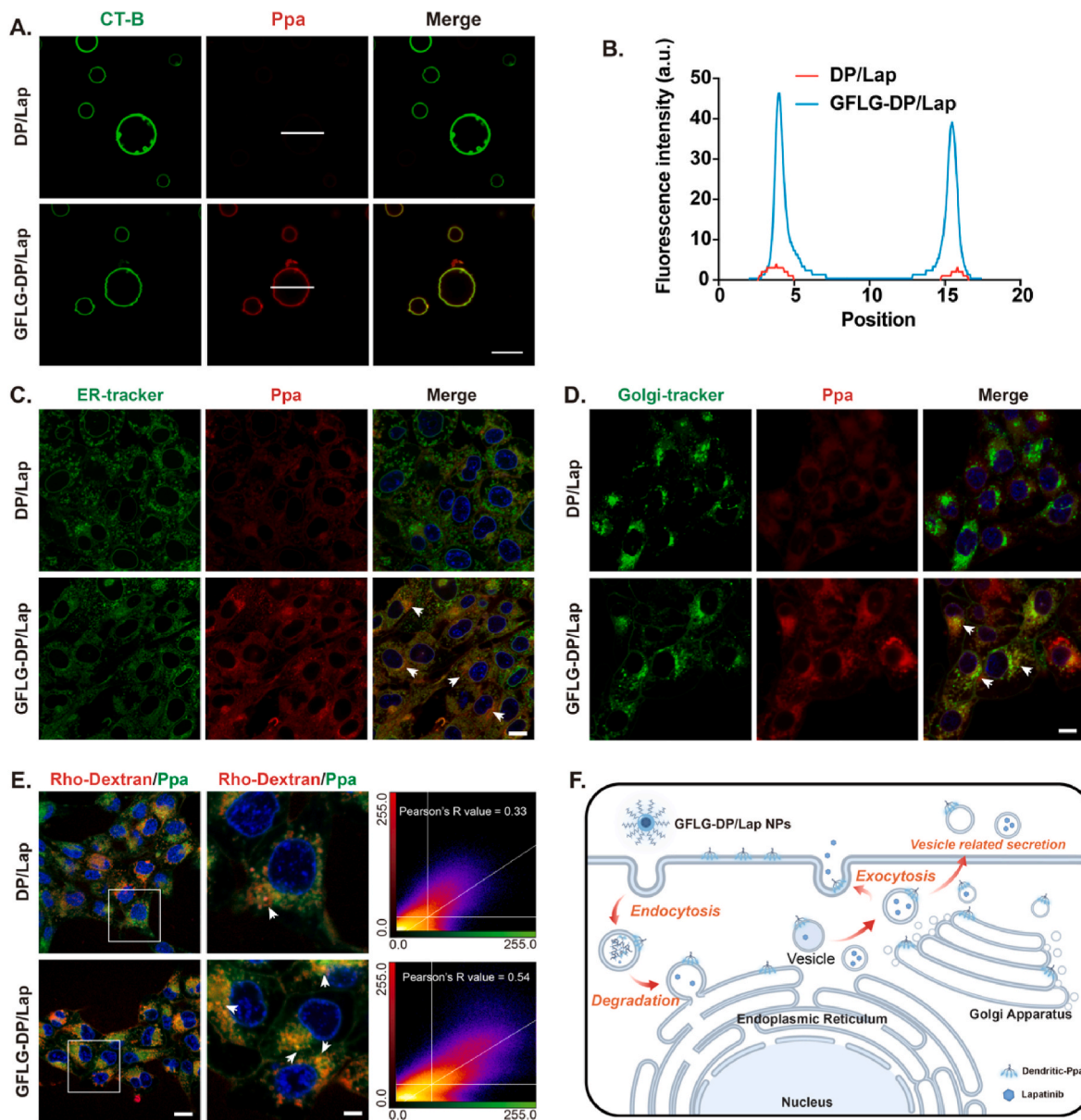


**Fig. 6.** (A): Ppa signal on GPMVs isolated from 4T1 cells incubated with DP/Lap NPs or GFLG-DP/Lap NPs under fluorescence microscopy. Red for Ppa signal and green for cholera toxin b (CT-B) subunit signal. Scale bar: 10 μm. (B): The Ppa fluorescence signal intensity of the membrane vesicles from cells treated with DP/Lap NPs and GFLG-DP/Lap NPs. (C, D): Confocal images for co-location of DP/Lap NPs or GFLG-DP/Lap NPs with the ER or GA in 4T1 cells. Red for Ppa signal, green for ER or GA signal. Scale bar: 10 μm. (E): Confocal images for co-location of DP/Lap NPs or GFLG-DP/Lap NPs with rhodamine-dextran (rho-dextran 70 kDa) in 4T1 cells. Green for Ppa signal, red for rho-dextran signal. The Pearson's R value of two enlarged areas are 0.33 (DP/Lap) and 0.54 (GFLG-DP/Lap), respectively. (F): Schematic diagram for the transportation of GFLG-DP/Lap NPs in tumor cells via the membrane activity.

released Ppa is sparsely distributed throughout the MTs. Therefore, the fluorescence signal of Ppa and the DESI-MSI signal of Lap are distributed throughout the MTs, confirming GFLG-DP/Lap NPs have the ability to achieve deep drugs penetration and great accumulation in

solid tumors.

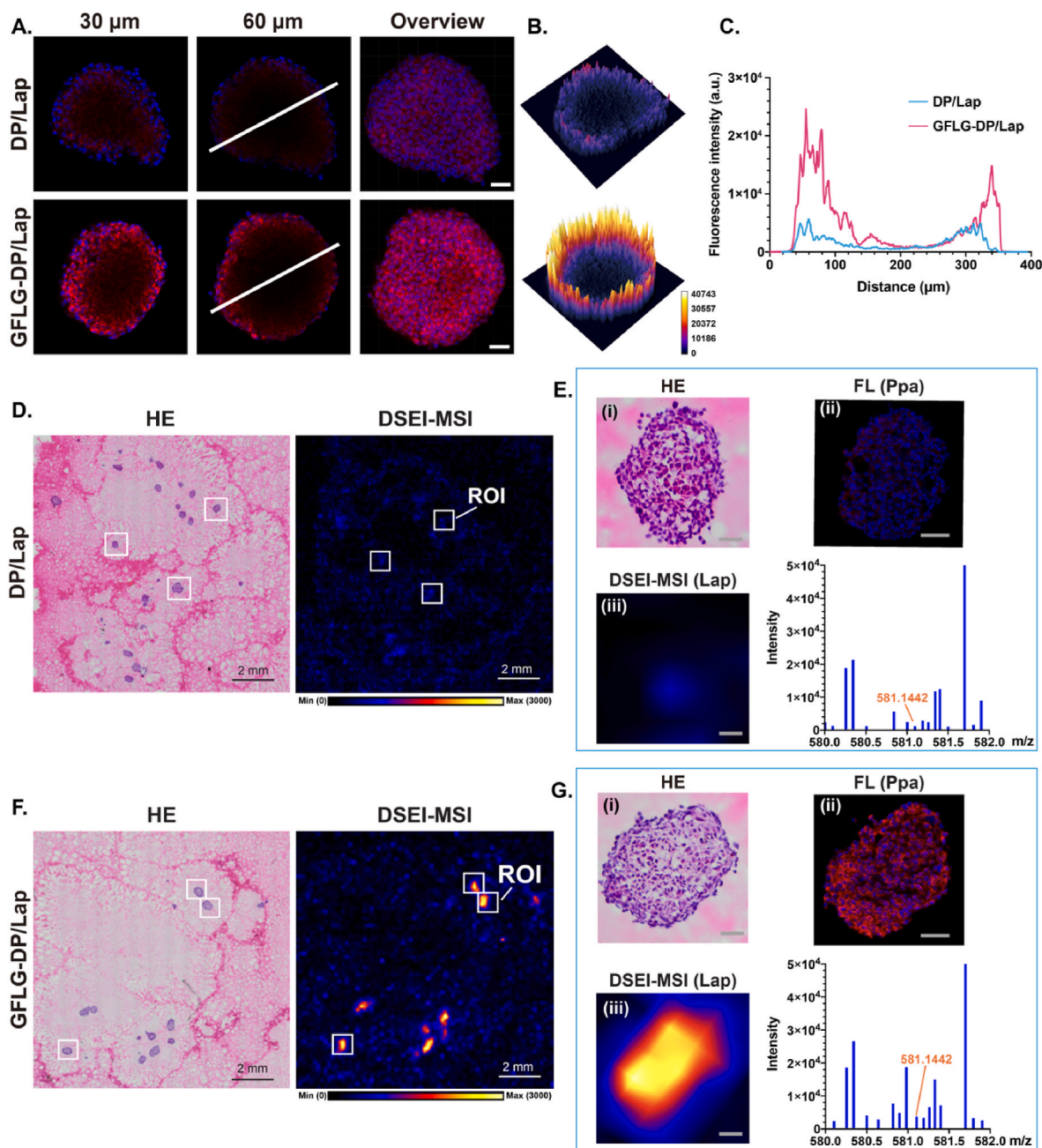


**Fig. 7.** (A): CLSM images of the sections of MTSs at a depth of 30 and 60  $\mu\text{m}$  after the treatment with DP/Lap or GFLG-DP/Lap NPs (5  $\mu\text{g}$  equivalent Ppa/mL). Red for Ppa signal. Scale bar: 50  $\mu\text{m}$ . (B): Fluorescence intensity of Ppa distributed in the MTS section at a depth of 60  $\mu\text{m}$ . (C): Ppa fluorescence intensity along the write lines in (A). (D): H&E staining image and DESI-MSI of a MTS section for Lap deposition in the DP/Lap NPs-treated MTS. Scale bar: 2 mm; pixel size, 100  $\mu\text{m} \times 100 \mu\text{m}$ . (E): (i) H&E staining image of the region of interest (ROI), (ii) fluorescence image of ROI for distribution of Ppa within the 4T1 MTS, (iii) DESI-MSI of ROI for distribution of Lap within the 4T1 MTS and DESI-MSI spectrum with the Lap peak ( $m/z = 581.1442$  for  $[\text{M}+\text{H}]^+$ ). Scale bar: 50  $\mu\text{m}$ . (F): H&E staining image and DESI-MSI of a MTS section for Lap deposition in the GFLG-DP/Lap NPs-treated MTS. Scale bar: 2 mm; pixel size, 100  $\mu\text{m} \times 100 \mu\text{m}$ . (G): (i) H&E staining image of the ROI, (ii) fluorescence image of ROI for the distribution of Ppa within the 4T1 MTS, (iii) DESI-MSI of ROI for the distribution of Lap within the 4T1 MTS and DESI-MSI spectrum with the Lap peak ( $m/z = 581.1442$  for  $[\text{M}+\text{H}]^+$ ). Scale bar: 50  $\mu\text{m}$ .

## 2.6. Excellent pharmacokinetics, deep penetration and long-term retention of GFLG-DP/Lap NPs in vivo

Insufficient accumulation, low cellular uptake, poor penetration and retention of nanomedicines at tumor sites are the challenging obstacles [44,45]. To explore the extravasation ability of the GFLG-DP/Lap NPs through tumor blood vessels, we built a tumor model and labeled the tumor blood vessels with fluorescein isothiocyanate (FITC)-dextran to observe the distribution of the nanomedicine within the tumor tissue by CLSM [46]. After 2 h of injection of DP/Lap NPs or GFLG-DP/Lap NPs

into tumor-bearing mice, we observe that the fluorescent signal of DP/Lap NPs does not spread to the entire tumor tissue. However, the red fluorescent signal of GFLG-DP/Lap NPs is extensively detected in the distal region of tumor vessels and these NPs are enriched in tumor cells (Fig. 8A). These results confirm that GFLG-DP-mediated drug delivery can effectively extravasate from the tumor vasculature into the distal tissues, while the drug in the GFLG-DP system can be rapidly internalized by tumor cells, thereby promoting its therapeutic action against tumor cells.

In addition, we examined Ppa accumulation from free Ppa, DP/Lap

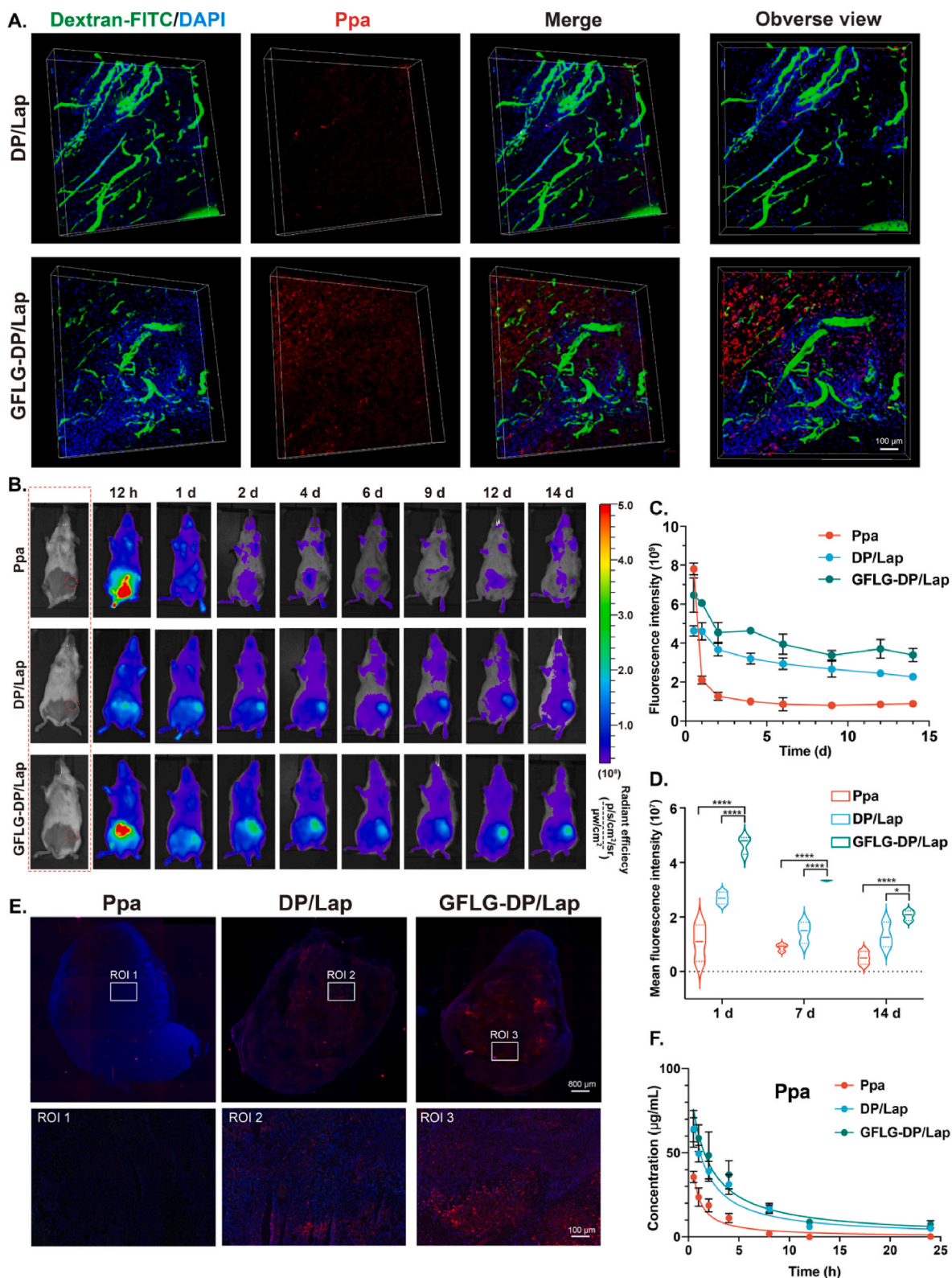


**Fig. 8.** (A): CLSM images for extravasation of DP/Lap NPs or GFLG-DP/Lap NPs from tumor vessels. Tumor vessels were labeled by FITC-dextran. Red for Ppa signal and green for FITC-dextran signal. Scale bar: 100  $\mu\text{m}$ . (B): Accumulation of free Ppa, DP/Lap NPs and GFLG-DP/Lap NPs at tumor sites via an *in vivo* imaging system (red circles). (C): Temporal changes in the fluorescence intensity at the tumor sites from fluorescence images in (B) ( $n = 3$ ). (D): MFI of harvested tumors from mice after injection of free Ppa, DP/Lap NPs or GFLG-DP/Lap NPs on day 1, 7 and 14 via *ex vivo* imaging ( $n = 3$ ).  $*P < 0.05$  and  $****P < 0.0001$ . (E): Accumulation of free Ppa, DP/Lap or GFLG-DP/Lap NPs in the tumor mass on day 14 after administration of these formulations. Scale bar: 800  $\mu\text{m}$ . The bottom row shows the enlarged images in the selected region in the top row. Scale bar: 100  $\mu\text{m}$ . (F): Plasma concentration-time curves of Ppa in the mice after intravenous injection of free Ppa, DP/Lap NPs or GFLG-DP/Lap NPs (5.0 mg equivalent Ppa/kg mice,  $n = 3$ ).

NPs and GFLG-DP/Lap NPs at the tumor site in the tumor-bearing mice. After intravenous administration with different formulations into the mice, the fluorescence intensity at the tumor site was monitored at different durations post-injection via an IVIS imaging system. The results show that GFLG-DP/Lap NPs retain at the tumor site with distinguished fluorescent intensity during two-week periods, which has great potential in extending the therapeutic effects of the drug incorporated inside GFLG-DP NPs on cancer cells (Fig. 8B and C). Meanwhile, *Ex vivo* imaging results confirm that the fluorescence intensity of Ppa in the tumors on day 14 post administration is very high in the GFLG-DP/Lap NPs-treated group, which is 1.5-fold higher than that in the DP/Lap NPs-treated group (Fig. 8D and S28). These results are supported from the CLSM images in the corresponding tumor sections, and the Ppa signal of GFLG-DP/Lap NPs is much stronger than that of DP/Lap NPs at the tumor tissue (Fig. 8E). Meanwhile, H&E staining of organs (heart, liver, spleen and kidney) reveals no significant changes in the structure of these organs after different treatments (Fig. S29). Thereby, GFLG-DP NPs can significantly improve drug accumulation, penetration and retention in tumors, which outperforms their corresponding control without enzyme responsiveness.

Furthermore, we investigated the pharmacokinetic profile of GFLG-DP/Lap NPs during blood circulation after their intravenous administration. The temporal plasma concentration profiles of Ppa are presented in Fig. 8F. The retention time of Ppa in DP/Lap NPs and GFLG-DP/Lap NPs during blood circulation is significantly prolonged compared to free Ppa, and the fluorescence signal of Ppa in the NPs is still detectable in the blood at 24 h post-injection. However, free Ppa is rapidly cleared from the blood, and cannot be detected at 12 h post injection. The pharmacokinetic characteristics of NPs are in alignment with the tumor accumulation results. These results indicate that DP/Lap NPs and GFLG-DP/Lap NPs can exhibit longer blood circulation than free drugs.

### 3. Conclusion

In conclusion, enzyme-triggered co-delivery of dual drugs from a nanomedicine into deep tumor tissues is realized by increasing the cell membrane activity to improve the tumor inhibition rate and prolong the survival of tumor-bearing mice via a combination therapeutic effect of inducing tumor apoptosis and inhibiting proliferation of tumor cells. First, GFLG-DP/Lap NPs with a long circulation time and excellent pharmacokinetic properties accumulate in the tumor via the EPR effect. Second, in response to CTSB overexpressed in tumor tissues and cells, GFLG-DP/Lap NPs release dendritic-Ppa, which binds to the membrane system and stimulates the membrane activity. Third, dendritic-Ppa and Lap are sparsely distributed throughout the entire tumor tissue and internalized by tumor cells via the vesicle activity. Lastly, dendritic-Ppa and Lap exert their therapeutic actions by inducing tumor apoptosis and inhibiting proliferation after laser irradiation, thus achieving a synergistically efficacious anti-tumor effect. The strategy for delivery of co-loaded drugs in a nanomedicine into deep tumor sites via membrane flow effectively addresses the limitations of the ROS therapeutic treatment model, and it could help develop emerging anti-tumor nanotherapeutics via perturbing the plasma membranes to achieve their deep penetration and high accumulation in the solid tumors.

### 4. Experimental section

Materials, methods, preparation and characterizations of the nanoparticles, cells, animal and imaging studies, *in vitro* and *in vivo* anticancer and their anticancer mechanism studies, and statistical analysis were provided in Supporting Information.

### CRedit authorship contribution statement

**Lei Gu:** Conceptualization, Methodology, Formal analysis, Investigation, Writing – original draft, Visualization. **Zhenyu Duan:**

Conceptualization, Methodology, Formal analysis, Investigation, Writing – original draft, Visualization, Funding acquisition. **Xue Li:** Methodology, Formal analysis. **Xin Li:** Methodology, Formal analysis. **Yinggang Li:** Methodology, Visualization. **Xiaoling Li:** Methodology, Investigation. **Gang Xu:** Methodology, Formal analysis, Investigation. **Peng Gao:** Methodology, Formal analysis, Investigation. **Hu Zhang:** Writing – review & editing. **Zhongwei Gu:** Supervision, Project administration. **Jie Chen:** Supervision, Funding acquisition, Project administration. **Qiyong Gong:** Supervision, Funding acquisition, Project administration. **Kui Luo:** Supervision, Funding acquisition, Project administration, Resources, Writing – review & editing.

### Declaration of competing interest

The authors declare that they have no known conflicts of Interest/competing interests, competing financial interests or personal relationships that could have appeared to influence the work reported in this paper.

### Acknowledgements

Lei Gu and Zhenyu Duan contributed equally to this work. The authors would like to thank Guiping Yuan for her help of TEM images, and Zhiqian Li, Lili Pan, Xiangyi Ren, Bo Su, Lin Bo, Lei Wu and Yaping Wu (Histology and Imaging Platform, Research Core Facility, West China Hospital, Sichuan University) for their help in imaging studies. The authors also acknowledge Qiaorong Huang and Wentong Meng (Laboratory of Stem Cell Biology, West China Hospital, Sichuan University) for help in flow cytometer. Figs. 1, 4L and 6F of contents entry were created with BioRender.com. This work was supported by National Natural Science Foundation of China (52073193, 51873120, 81621003, 52203182, 32071284), National Key Research and Development Program of China (2022YFC2009900), 1-3-5 Project for Disciplines of Excellence, West China Hospital, Sichuan University (ZYJC21013), Research Funds in West China Hospital of Sichuan University (2020HXBH072), and China Postdoctoral Science Foundation (2019TQ0220, 2022M712225, 2022T150446).

### Appendix A. Supplementary data

Supplementary data to this article can be found online at <https://doi.org/10.1016/j.bioactmat.2023.02.015>.

### References

- [1] D. Zhou, L. Shao, D.R. Spitz, Reactive oxygen species in normal and tumor stem cells, *Adv. Cancer Res.* 122 (2014) 1–67, <https://doi.org/10.1016/B978-0-12-420117-0.00001-3>.
- [2] M.L. Circu, T.Y. Aw, Reactive oxygen species, cellular redox systems, and apoptosis, *Free Radic. Biol. Med.* 48 (2010) 749–762, <https://doi.org/10.1016/j.freeradbiomed.2009.12.022>.
- [3] H. Sies, D.P. Jones, Reactive oxygen species (ROS) as pleiotropic physiological signalling agents, *Nat. Rev. Mol. Cell Biol.* 21 (2020) 363–383, <https://doi.org/10.1038/s41580-020-0230-3>.
- [4] Z.L. Li, et al., A tumor cell membrane-coated self-amplified nanosystem as a nanovaccine to boost the therapeutic effect of anti-PD-L1 antibody, *Bioact. Mater.* 21 (2023) 299–312, <https://doi.org/10.1016/j.bioactmat.2022.08.028>.
- [5] C. Zhang, X. Wang, J. Du, Z. Gu, Y. Zhao, Reactive oxygen species-regulating strategies based on nanomaterials for disease treatment, *Adv. Sci.* 8 (2021), 2002797, <https://doi.org/10.1002/advs.202002797>.
- [6] P. Tan, et al., Artificial intelligence aids in development of nanomedicines for cancer management, *Semin. Cancer Biol.* 89 (2023) 61–75, <https://doi.org/10.1016/j.semcancer.2023.01.005>.
- [7] Z. Duan, et al., Synergistic Therapy of a naturally inspired glycopolymer-based biomimetic nanomedicine harnessing tumor genomic instability, *Adv. Mater.* 33 (2021), 2104594, <https://doi.org/10.1002/adma.202104594>.
- [8] X. Cheng, et al., Multi-functional liposome: a powerful theranostic nano-platform enhancing photodynamic therapy, *Adv. Sci.* 8 (2021), e2100876, <https://doi.org/10.1002/advs.202100876>.
- [9] R. Canaparo, F. Foglietta, N. Barbero, L. Serpe, The promising interplay between sonodynamic therapy and nanomedicine, *Adv. Drug Deliv. Rev.* 189 (2022), 114495, <https://doi.org/10.1016/j.addr.2022.114495>.

- [10] D. Lee, et al., Overcoming the obstacles of current photodynamic therapy in tumors using nanoparticles, *Bioact. Mater.* 8 (2022) 20–34, <https://doi.org/10.1016/j.bioactmat.2021.06.019>.
- [11] J.M. Chen, et al., Advances in nanomaterials for photodynamic therapy applications: status and challenges, *Biomaterials* 237 (2020), 119827, <https://doi.org/10.1016/j.biomaterials.2020.119827>.
- [12] Q. Zhou, et al., Enzyme-activatable polymer-drug conjugate augments tumour penetration and treatment efficacy, *Nat. Nanotechnol.* 14 (2019) 799–809, <https://doi.org/10.1038/s41565-019-0485-z>.
- [13] M.J. Mitchell, et al., Engineering precision nanoparticles for drug delivery, *Nat. Rev. Drug Discov.* 20 (2020) 101–124, <https://doi.org/10.1038/s41573-020-0090-8>.
- [14] H. Tsukagoshi, W. Busch, P.N. Benfey, Transcriptional regulation of ROS controls transition from proliferation to differentiation in the root, *Cell* 143 (2010) 606–616, <https://doi.org/10.1016/j.cell.2010.10.020>.
- [15] K.B. Myant, et al., ROS production and NF-kappaB activation triggered by RAC1 facilitate WNT-driven intestinal stem cell proliferation and colorectal cancer initiation, *Cell Stem Cell* 12 (2013) 761–773, <https://doi.org/10.1016/j.stem.2013.04.006>.
- [16] R. Mittler, ROS are good, *Trends Plant Sci.* 22 (2017) 11–19, <https://doi.org/10.1016/j.tplants.2016.08.002>.
- [17] L. Diebold, N.S. Chandel, Mitochondrial ROS regulation of proliferating cells, *Free Radic. Biol. Med.* 100 (2016) 86–93, <https://doi.org/10.1016/j.freeradbiomed.2016.04.198>.
- [18] J. Ridgway, et al., Inhibition of Dll4 signalling inhibits tumour growth by deregulating angiogenesis, *Nature* 444 (2006) 1083–1087, <https://doi.org/10.1038/nature05313>.
- [19] P. Wee, Z. Wang, Epidermal growth factor receptor cell proliferation signaling pathways, *Cancers* 9 (5) (2017) 52, <https://doi.org/10.3390/cancers9050052>.
- [20] M.K. Ediriweera, K.H. Tennekoon, S.R. Samarakoon, Role of the PI3K/AKT/mTOR signaling pathway in ovarian cancer: biological and therapeutic significance, *Semin. Cancer Biol.* 59 (2019) 147–160, <https://doi.org/10.1016/j.semcancer.2019.05.012>.
- [21] Y. Wang, Z. Lv, F. Chen, X. Wang, S. Gou, Conjugates derived from lapatinib derivatives with cancer cell stemness inhibitors effectively reversed drug resistance in triple-negative breast cancer, *J. Med. Chem.* 64 (2021) 12877–12892, <https://doi.org/10.1021/acs.jmedchem.1c01013>.
- [22] A.M. Goodman, et al., Near-infrared remotely triggered drug-release strategies for cancer treatment, *Proc. Natl. Acad. Sci. U.S.A.* 114 (2017) 12419–12424, <https://doi.org/10.1073/pnas.1713137114>.
- [23] S.Y. Lee, H.J. Cho, Mitochondria targeting and destabilizing hyaluronic acid derivative-based nanoparticles for the delivery of lapatinib to triple-negative breast cancer, *Biomacromolecules* 20 (2019) 835–845, <https://doi.org/10.1021/acs.biomac.8b01449>.
- [24] A. Franovic, et al., Translational up-regulation of the EGFR by tumor hypoxia provides a nonmutational explanation for its overexpression in human cancer, *Proc. Natl. Acad. Sci. U.S.A.* 104 (2007) 13092–13097, <https://doi.org/10.1073/pnas.0702387104>.
- [25] Y. Shen, et al., EGFR modulates microRNA maturation in response to hypoxia through phosphorylation of AGO2, *Nature* 497 (2013) 383–387, <https://doi.org/10.1038/nature12080>.
- [26] M. Mamo, et al., Hypoxia alters the response to anti-EGFR therapy by regulating EGFR expression and downstream signaling in a DNA methylation-specific and HIF-dependent manner, *Cancer Res.* 80 (2020) 4998–5010, <https://doi.org/10.1158/0008-5472.CAN-20-1232>.
- [27] S. Kuang, et al., A Mitochondrion-localized two-photon photosensitizer generating carbon radicals against hypoxic tumors, *Angew. Chem. Int. Ed.* 59 (2020) 20697–20703, <https://doi.org/10.1002/anie.202009888>.
- [28] H. Zhou, et al., Hypoxia-triggered self-assembly of ultrasmall iron oxide nanoparticles to amplify the imaging signal of a tumor, *J. Am. Chem. Soc.* 143 (2021) 1846–1853, <https://doi.org/10.1021/jacs.0c10245>.
- [29] D.C. Singleton, A. Macann, W.R. Wilson, Therapeutic targeting of the hypoxic tumour microenvironment, *Nat. Rev. Clin. Oncol.* 18 (2021) 751–772, <https://doi.org/10.1038/s41571-021-00539-4>.
- [30] A. Sharma, et al., Hypoxia-targeted drug delivery, *Chem. Soc. Rev.* 48 (2019) 771–813, <https://doi.org/10.1039/c8cs00304a>.
- [31] W. Yan, et al., Anti-hypoxia nanosized drug delivery systems improving cancer therapy, *Nano Today* 42 (2022), 101376, <https://doi.org/10.1016/j.nantod.2022.101376>, 2022.
- [32] L. Gu, et al., A Transformable Amphiphilic and block polymer-dendron conjugate for enhanced tumor penetration and retention with cellular homeostasis perturbation via membrane flow, *Adv. Mater.* 34 (2022), e2200048, <https://doi.org/10.1002/adma.202200048>.
- [33] M.D. Liu, et al., A transistor-like pH-sensitive nanodetergent for selective cancer therapy, *Nat. Nanotechnol.* 17 (2022) 541–551, <https://doi.org/10.1038/s41565-022-010185-5>.
- [34] C. Peetla, S. Vijayaraghavalu, V. Labhasetwar, Biophysics of cell membrane lipids in cancer drug resistance: implications for drug transport and drug delivery with nanoparticles, *Adv. Drug Deliv. Rev.* 65 (2013) 1686–1698, <https://doi.org/10.1016/j.addr.2013.09.004>.
- [35] M. Wu, et al., Activation of pyroptosis by membrane-anchoring AIE photosensitizer design: new prospect for photodynamic cancer cell ablation, *Angew. Chem. Int. Ed.* 133 (2021) 9175–9180, <https://doi.org/10.1002/ange.202016399>.
- [36] H. Cai, et al., Stimuli-sensitive linear-dendritic block copolymer-drug prodrug as a nanoplatform for tumor combination therapy, *Adv. Mater.* 34 (2022), e2108049, <https://doi.org/10.1002/adma.202108049>.
- [37] H.N. Li, et al., Recent advances in development of dendritic polymer-based nanomedicines for cancer diagnosis, *WIREs Nanomed. Nanobiotechnol.* 13 (2021), <https://doi.org/10.1001/wnan.1670>.
- [38] M. Tian, et al., Liposome-based nanoencapsulation of a mitochondria-stapling photosensitizer for efficient photodynamic therapy, *ACS Appl. Mater. Interfaces* 14 (2022) 12050–12058, <https://doi.org/10.1021/acsami.1c23156>.
- [39] S. Chen, et al., Enhanced tumour penetration and prolonged circulation in blood of polyzwitterion-drug conjugates with cell-membrane affinity, *Nat. Biomed. Eng.* 5 (2021) 1019–1037, <https://doi.org/10.1038/s41551-021-00701-4>.
- [40] Q. Luo, et al., Branched polymer-based redox/enzyme-activatable photodynamic nanoagent to trigger STING-dependent immune responses for enhanced therapeutic effect, *Adv. Funct. Mater.* 32 (2021), <https://doi.org/10.1002/adfm.202110408>.
- [41] S. Guenther, et al., Spatially resolved metabolic phenotyping of breast cancer by desorption electrospray ionization mass spectrometry, *Cancer Res.* 75 (2015) 1828–1837, <https://doi.org/10.1158/0008-5472.CAN-14-2258>.
- [42] D. Calligaris, et al., Application of desorption electrospray ionization mass spectrometry imaging in breast cancer margin analysis, *Proc. Natl. Acad. Sci. U.S.A.* 111 (2014) 15184–15189, <https://doi.org/10.1073/pnas.1408129111>.
- [43] X. Song, Q. Zang, R.N. Zare, Hydrogen-deuterium exchange desorption electrospray ionization mass spectrometry visualizes an acidic tumor microenvironment, *Anal. Chem.* 93 (2021) 10411–10417, <https://doi.org/10.1021/acs.analchem.1c02026>.
- [44] Q. Sun, Z. Zhou, N. Qiu, Y. Shen, Rational design of cancer nanomedicine: nanoproperty integration and synchronization, *Adv. Mater.* 29 (2017), <https://doi.org/10.1002/adma.201606628>.
- [45] K. Yang, et al., Polyprodrug nanomedicines: an emerging paradigm for cancer therapy, *Adv. Mater.* 34 (2022), e2107434, <https://doi.org/10.1002/adma.202107434>.
- [46] R.D. Field, et al., Ultrasound-responsive aqueous two-phase microcapsules for on-demand drug release, *Angew. Chem. Int. Ed.* 61 (2022), 202116515, <https://doi.org/10.1002/anie.202116515>.